Full length article

An informatics approach to transformation temperatures of NiTi-based shape memory alloys

Dezhen Xue [a, b, *], Deqing Xue [a], Ruihao Yuan [a], Yumei Zhou [a], Prasanna V. Balachandran [b], Xiangdong Ding [a], Jun Sun [a], Turab Lookman [b, **]

[a] State Key Laboratory for Mechanical Behavior of Materials, Xi'an Jiaotong University, Xi'an 710049, China
[b] Theoretical Division, Los Alamos National Laboratory, Los Alamos, NM 87545, USA

ARTICLE INFO

ABSTRACT

The martensitic transformation serves as the basis for applications of shape memory alloys (SMAs). The ability to make rapid and accurate predictions of the transformation temperature of SMAs is therefore of much practical importance. In this study, we demonstrate that a statistical learning approach using three features or material descriptors related to the chemical bonding and atomic radii of the elements in the alloys, provides a means to predict transformation temperatures. Together with an adaptive design framework, we show that iteratively learning and improving the statistical model can accelerate the search for SMAs with targeted transformation temperatures. The possible mechanisms underlying the dependence of the transformation temperature on these features is discussed based on a Landau-type phenomenological model.

© 2016 Acta Materialia Inc. Published by Elsevier Ltd. All rights reserved.

1. Introduction

Martensitic transformations are solid-to-solid displacive transitions characterized by a spontaneous strain accompanying a rapid change of crystal structure at the transformation temperature [1]. Shape-memory alloys (SMAs), undergoing reversible martensitic phase transformations, are widely used in applications ranging from sensors, actuators, eco-friendly refrigerators to energy conversion devices [2—6]. Most SMA based devices utilize either the temperature-induced or stress-induced martensitic transformation, so that the transformation temperature determines the temperature window for device use [7—10] and is thus critical to applications of SMAs [1].

The transformation temperatures of SMAs are also strongly affected by their chemical composition [1,8—13]. As a result, the most common approach to tuning the transformation temperature for high or low temperature applications is to introduce elements to change the composition [14]. A number of studies have focused on adding ternary elements to commercially used $Ti_{50.0}Ni_{50.0}$ to modify its transformation temperature and have identified specific elements that can elevate or lower the transformation temperature [14]. Alloying elements, such as Fe, Cr, V, Mn and Co lower the transformation temperature [15,16], whereas Au, Pd, Pt, Zr and Hf, increase the temperature [12,14]. Moreover, the dependence of the martensitic transformation temperature on the concentration varies with the type of point defect. For example, in ternary alloys a 1.0 at% of Cr replacing Ni in $Ti_{50.0}Ni_{50.0}$ lowers the transformation temperature by more than 150 K, whereas for Co one needs more than 7.0 at% to decrease the transformation temperature by 150 K [14,17].

However, in many cases ternary alloys are unable to satisfy the application requirements and so quaternary or even multi-component alloys need to be considered for desired properties [18,19]. The increase in the number of elements is a serious impediment to developing SMAs with desired transformation temperatures as the chemical search space increases exponentially in size and complexity with alloying elements [19]. For $Ti_{50.0}Ni_{50.0}$ based alloys, the number of allowed candidate alloys can be as large as 10^6 if three elements, whose concentrations are measured to 0.1%, can replace Ni. This is too vast a space to search experimentally. A method which allows us to effectively explore the complex search space to reduce time and costs is thus crucially important.

* Corresponding author. State Key Laboratory for Mechanical Behavior of Materials, Xi'an Jiaotong University, Xi'an 710049, China.
** Corresponding author.
  E-mail addresses: xuedezhen@xjtu.edu.cn (D. Xue), txl@lanl.gov (T. Lookman).

From a practical point of view, desired are rapid and accurate predictions of the transformation temperatures based on different alloying elements and their concentrations.

Recently, there is growing interest in accelerating the materials discovery process of finding materials with targeted properties by reducing the number of costly and time-consuming trial and error experiments [19–26]. To this end, data-based statistical learning approaches are gradually making inroads into materials science. Some recent examples of informatics-driven design of new materials include predictions of molecular properties, transition states, structure classification of alloys, dielectric and piezoelectric properties and predictions of band gaps [19–26].

In the present work, we explore a data-driven methodology that involves applying statistical learning tools to analyze correlations between transformation temperatures in SMAs and several scalar descriptors or features of electronic and crystal structure parameters in the constrained pseudo-quaternary system, Ti_{50} ($Ni_{50-x-y-z}$ $Cu_x Fe_y Pd_z$). We have previously used this system to identify x,y,z in compounds with very low thermal hysteresis [19]. Our focus here is on developing a predictive data-driven capability to estimate the transformation temperature of unknown samples and to find alloys with targeted transformation temperatures in an accelerated manner. We find that a simple polynomial model, using three preselected material features or descriptors that capture chemical bonding and atomic size, works exceedingly well in describing the data. In this model, the transformation temperature depends linearly on the weighted average of the valence electron number (*ven*), Pauling electronegativity (*en*) and *quadratically* on Waber-Cromer's pseudopotential radius(*dor*) of the constituents of the alloys. Based on this relationship, we propose a simplified Landau-type model to understand the mechanism controlling the transformation temperatures in NiTi-based alloys. Using the statistical learning model together with an adaptive design framework, we show that iteratively learning and improving the model accelerates the search for SMAs with targeted high transformation temperatures. In particular, we show how our design strategy predicts that $Ti_{50} Ni_{25} Pd_{25}$ has the highest transition temperature of 189.56 °C in our restricted search space. Our experimental work validates this finding with a measured transformation temperature of 182.89 °C. Our methodology can be generalized to optimize other properties in multicomponent SMAs.

Our paper is organized as follows. In Sec. 2 and 3, we introduce the experimental methods, our target property and dataset. Sec. 4 describes how we choose the most relevant features to make a prediction. Sec. 5 compares different regression models and identifies the best one. In Sec. 6, we show how the adaptive design framework utilizes the regression model to accelerate the search for alloys with targeted transformation temperatures. And finally in Sec. 7, we discuss the underlying physics of the dependence of the transformation temperature on the pre-selected features, which relate to the chemical bonding and atomic radii of the alloying elements.

2. Experiments

In the present study, we focus on the effects of chemical composition of NiTi-based alloys on the martensitic transformation temperature. We synthesized samples under identical conditions to avoid the effects of microstructural parameters such as grain size, precipitates and dislocations on the transformation temperature. The base ingot for the $Ti_{50}(Ni_{50-x-y-z} Cu_x Fe_y Pd_z)$ alloy was made by arc melting from pure 99.9% Ti, 99.9% Ni, 99.9% Cu, 99.9% Fe and 99.9% Pd in an argon atmosphere. The ingot was hot-rolled into a 1.0 mm thick plate, the specimens for measurements were spark-

cut from the plate and then solution-treated at 1273 K for 1 h in an evacuated quartz tube, followed by water quenching. Differential scanning calorimetry (DSC) measurements were made with a cooling/heating rate of 10 K min^{-1} to determine the martensitic transformation temperatures using exothermal/endothermic peaks.

3. Dataset

An input training data set is needed in order to build a quantitative statistical learning model for the NiTi-based systems. Each material we are interested must be characterized or labelled via a representation in terms of one or more material descriptors or features, X. They represent aspects of structure, chemistry, bonding. Our machine learning method then learns a map or model connecting features X to a specific objective or material property Y (transformation temperature here), that is, $Y = f(X)$. Thus, two main ingredients of the machine learning approach are the empirical model, f and the features, X. The learning algorithm to estimate f must be trained and cross validated using a *training* dataset, which includes the measured targeted material property. The set of unexplored, possible materials whose targeted material properties have not been measured from the *virtual* dataset, on which f will be applied to predict or estimate the targeted property.

As shown in Fig. 1, we define an endothermic peak temperature, T_p, of the differential scanning calorimetry (DSC) curve as our target property for the transformation temperature. Other definitions such as M_s and M_f, the start and finish temperatures for the martensitic transformation, and A_s and A_f, the start and finish temperatures for the reverse transformation, could have also been adopted. We chose T_p for simplicity and accuracy. We considered $Ti_{50}(Ni_{50-x-y-z} Cu_x Fe_y Pd_z)$ alloys with x, y and z compositions, which can vary in steps of 0.1% with constraints $50 - x - y - z \leq 25\%$, $x \geq 20\%$, $y \geq 7\%$ and $z \geq 25\%$. This gives us 1,652,470 possibilities in all. Of these, we synthesized 53 and measured their T_p to form our *training* dataset, ensuring that the processing conditions were identical to minimize variability due to processing and microstructural effects. It is well known that changes in processing conditions affect microstructure (e.g. cast versus wrought gives rise to different microstructures in the case of the SMA Uranium Niobium). We tried to minimize this dependence on processing conditions so that the microstructural features would not vary as much across our samples and could be neglected as a first order effect. The remaining unexplored search space
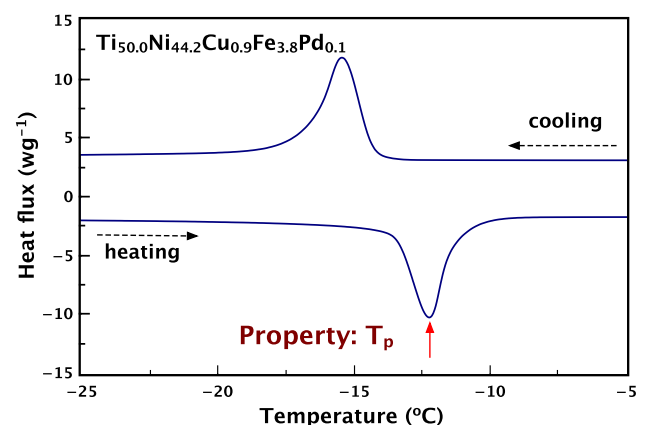

Fig. 1. Definition of the property. The endothermic peak of the differential scanning calorimetry (DSC) curve, T_p, is our targeted property to optimize. The typical DSC result shown is from $Ti_{50}(Ni_{44.2} Cu_{0.9} Fe_{3.8} Pd_{0.1})$, one of our alloys in the *training* data.

constitutes the *virtual* dataset, that is, 1,652,417 potential alloys with unknown transformation temperatures.

4. Feature selection

We discuss here how we choose the relevant features that form the input to the statistical learning model. A physical understanding of how the transformation temperature depends on composition has been the basis to intuitively screen the search space of SMA alloys and has been widely discussed in the literature [8–11,13]. For example, it is known that strong elastic softening, i.e., the decrease in elastic constant with temperature, occurs prior to the martensitic transformation and there is a critical value of the elastic constant at the transformation temperature [10]. Ren and Otsuka pointed out that the critical elastic constant is composition insensitive [11]. Therefore, the critical elastic constant can be reached at higher temperatures for softer materials and at lower temperatures for stiffer materials by tuning the composition. However, a direct mapping between the composition and the elastic properties is not available. Zarinejad and Liu subsequently associated the weighted average valence electron number (*ven*) with the elastic properties of SMAs and rationalized that the transformation temperature and *ven* are strongly correlated [8]. Frenzel et al. recently pointed out that the elastic constant is not sufficient by itself to predict the behavior of NiTi-based SMAs and suggested two factors controlling the transformation temperature: 1) a geometrical contribution as the result of changes in bonding by alloying elements; and 2) an intrinsic instability of the parent phase, which is related to the electronic structure [9].

Thus, the features we used comprised the set: Pauling electronegativity (*en*), metallic radius (*mr*), valence electron number (*ven*), Waber-Cromer's pseudopotential radii (*dor*), Clementi's atomic radii (*arc*), and Pettifor chemical scale (*cs*) [27–32]. These features represent a coarse-grained analogue of electronic, bonding and radii properties in SMAs and provide a relatively simple physical basis for modeling structure-property relationship for the transformation temperature. Another consideration is that the material descriptors or features should be easily accessible for all possible materials, irrespective of the desired properties. The features, X, for each $Ti_{50}(Ni_{50-x-y-z} Cu_x Fe_y Pd_z)$ alloy in our composition space were uniquely described as a weighted fraction of the elemental features, that is,

$$X = f_{Ti}X^{Ti} + f_{Ni}X^{Ni} + f_{Cu}X^{Cu} + f_{Fe}X^{Fe} + f_{Pd}X^{Pd}, \quad (1)$$

where $f_{Ti}, f_{Ni}, f_{Cu}, f_{Fe}$ and f_{Pd} are the atomic fractions of each element, $X^{Ti}, X^{Ni}, X^{Cu}, X^{Fe}$ and X^{Pd} are the corresponding features of each element. Furthermore, Zarinejad and Liu also associated the transformation temperatures of SMAs with the average concentration of valence electrons which can be defined as the ratio of the number of valence electrons to the total number of electrons of the alloy (the atomic number) [8]. They observed a clear linear correlation between the transformation temperature and the average concentration of valence electrons [8]. Thus, we also define the ratio of each feature X to the atomic number for each alloy to yield a new feature given by

$$cX = \frac{f_{Ti}X^{Ti} + f_{Ni}X^{Ni} + f_{Cu}X^{Cu} + f_{Fe}X^{Fe} + f_{Pd}X^{Pd}}{f_{Ti}Z^{Ti} + f_{Ni}Z^{Ni} + f_{Cu}Z^{Cu} + f_{Fe}Z^{Fe} + f_{Pd}Z^{Pd}}, \quad (2)$$

where $Z^{Ti}, Z^{Ni}, Z^{Cu}, Z^{Fe}$ and Z^{Pd} are the atomic numbers of each element. Table 1 lists all the features we used in the present study.

It is often the case that some or many of the features used in statistical learning models are not directly associated with the

Table 1
List of features used.

Abbreviation	Description	Ref.
Numa	number of elements	
Cs	Pettifor chemical scale	[29]
Arc	Clementi's atomic radii	[31]
En	Pauling electronegativity	[27]
Ven	Valence electron numbers	[32]
Mr	metallic radius	[30]
dor	Waber-Cromer's pseudopotential radii	[28]
anum	atomic number	
mass	atomic mass	
ccs	average concentration of *cs*	
carc	average concentration of *arc*	
cmr	average concentration of *mr*	
cen	average concentration of *en*	
cven	average concentration of *ven*	
cdor	average concentration of *dor*	
cmass	average concentration of *mass*	

targeted property. Usually, including such features increases the dimensionality of the feature space and leads to unnecessary complexity in the resulting model. By removing these features, we are usually left with a simpler model, the results of which are then easier to interpret. Initially, features which are themselves highly correlated can be considered to contain essentially similar information. Therefore, we subject these features to a correlation filter to remove those that are uncorrelated to them. The Pearson correlation map is very useful for this purpose and is presented in Fig. 2. It is calculated using the training data of 53 measurements with blue and red colors indicating positive and negative correlations, respectively. The lighter the tone, the less significant is the corresponding correlation. In the upper-right half, the filled fraction of circles in each of the pie charts corresponds to the absolute value of the associated Pearson correlation coefficient. Two clusters of data can be identified from the correlation map. In the right-bottom corner, *ccs*, *carc*, *cmr*, *cen*, *cven*, *cmass* and *cdor* are highly correlated. Thus we choose *ccs* to be typical of the information from this set of features. Another cluster present is that with *mr*, *en*, *arc*, *anum*, *mass* and *dor*. As they are all correlated, we selected *mr*, *en* and *dor* as representative of these features. Thus, after the correlation filter to down select features, we retain a subset of seven features that includes *numa*, *cs*, *mr*, *en*, *ven*, *dor* and *ccs*. Our preference for choosing mr, en and dor was dictated by the fact that these features are more specific and physically meaningful in terms of their influence on SMA properties than just *anum*, *mass* and *arc*. The latter are rather general and some of them (e.g the radii) are essentially captured by other features in the set. Also, *ven* and *cs* directly influence electronic properties whereas *cmass* and *cdor* are less specific in terms of their impact. Also, the clustering appears to reflect aspects of the training data primarily characterized by the different radii or electronic structure properties. However, the exact cause of this clustering is difficult to decipher from merely this type of analysis.

To further screen the features, we utilized the so-called *subset selection* method, which identifies a subset of the features that are mostly related to the targeted property [33]. If we have *p* features, we fitted a separate least squares regression model for each possible combination of those features. For example, we can fit *p* models which contain only one feature, and can fit p(p − 1)/2 models which contain two features, and so forth. We then compared the performance of all the resulting models and identified the best one. The application of *best subset selection* to our problem is shown in Fig. 3. Each plotted point corresponds to a *least squares regression* model fit using a different subset of the 7 features and the x-axis denotes the number of features used to fit the model.
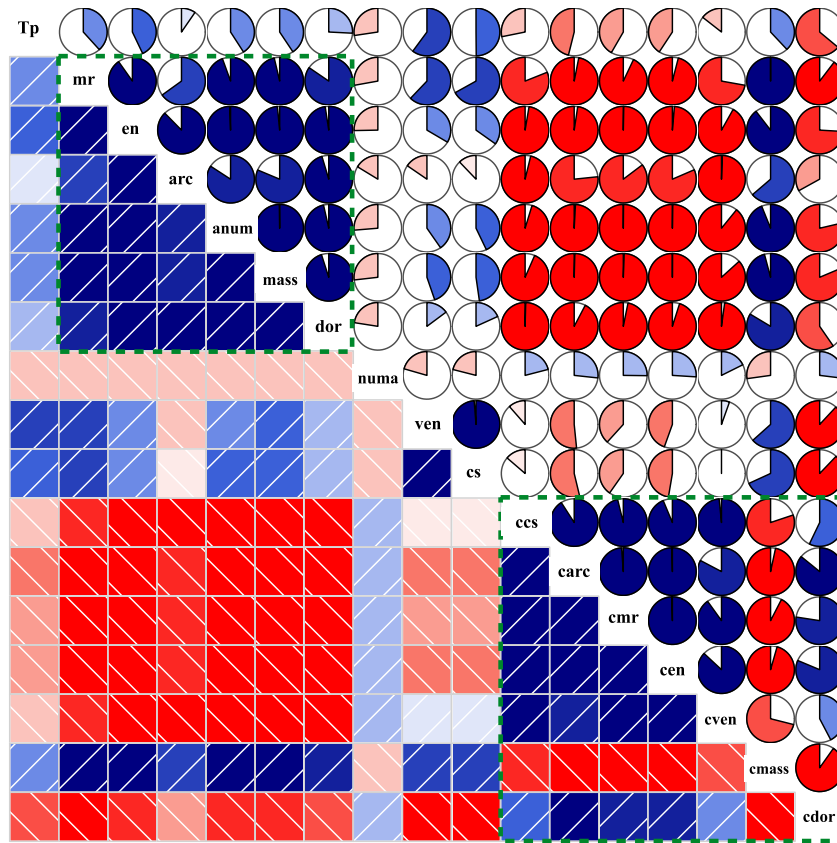
Fig. 2. Pearson correlation map for features. A graphical representation of the Pearson correlation matrix for the initial features. Blue and red colors indicate positive and negative correlations, respectively. The lighter the tone used, the less significant is the corresponding correlation. The filled fraction of the circle in each of the pie charts corresponds to the absolute value of the associated Pearson correlations coefficient. (For interpretation of the references to colour in this figure legend, the reader is referred to the web version of this article.)
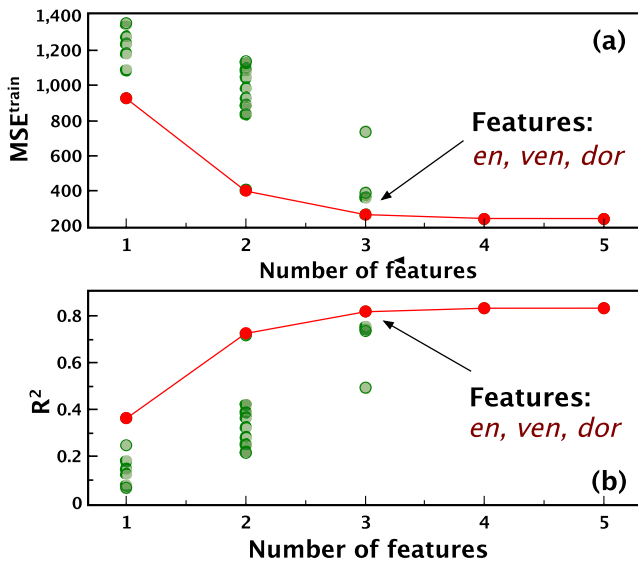

Fig. 3. The mean squared error (MSE^{train}) and R^2 of each possible linear model containing a subset of the seven features in our training data. The red frontier tracks the best model for a given number of features, according to MSE^{train} and R^2. Both MSE^{train} and R^2 show little improvement beyond 3 features. Thus, the subset of 3 features we employ includes *en*, *ven* and *dor*. (For interpretation of the references to colour in this figure legend, the reader is referred to the web version of this article.)

Fig. 3 shows the mean squared error (*MSE*) and R^2 statistics for each model as a function of the number of features used to fit the model.

The *MSE* captures the difference between the model predicted value, ($\widehat{y}_i$) and measured value (y_i), and is given by,

$$MSE^{train} = \frac{1}{n} \sum_{i=1}^{n} (y_i - \widehat{y}_i)^2. \tag{3}$$

The smaller the MSE^{train}, the better we expect the model performance to be. The R^2 is an alternative measure of the performance and is given by

$$R^2 = 1 - \frac{\sum_{i=1}^{n} (y_i - \widehat{y}_i)}{\sum_{i=1}^{n} (y_i - \overline{y})}, \tag{4}$$

where $\overline{y}$ is the mean value of y_i. The R^2 value lies between 0 and 1, with 1 signifying excellent fits. In Fig. 3, the red frontier lines connect the best models for each model size, according to MSE^{train} and R^2 and we see that the two quantities improve as the number of features increases. However, there is little improvement in MSE^{train} and R^2 beyond the use of 3 features, hence we limit ourselves to three in the subsequent statistical learning process. The best subset of 3 features includes *en*, *ven* and *dor*, and we use them to estimate the statistical learning models f for $T_p = f(en, ven, dor)$. Our full training data set including features and known transition temperatures are given in Appendix A and B.

5. Regression models

Our objective is to learn a quantitative relationship between a material property, (Y, transformation temperature) and the features characterizing the material (X), i.e. $Y = f(X)$. In general f is unknown but statistical inference provides a means to estimate f. In the following, we estimate f by using regression methods including linear (LIN) and polynomial regression (POLY), support vector regression with a linear kernel (SVR.lin), polynomial kernel (SVR.poly) and radial basis function kernel (SVR.rbf). These approaches identify how the response T_p varies with *en*, *ven*, and *dor*. As the set of features, *en*, *ven*, and *dor* are readily available, our learning approaches can yield accurate predictions for the targeted property, T_p, for all the unexplored data, as well as a way to understand how T_p is affected by *en*, *ven*, and *dor*.

5.1. Statistical learning models

Estimating f by linear regression (LIN) is a straightforward method for establishing a linear relationship between X and Y. For our problem, we can write this relationship as

$$T_p = \beta_0 + \beta_1 en + \beta_2 dor + \beta_3 ven, \qquad (5)$$

where β_i are the coefficients for different features, which can be estimated by the method of least squares. The performance of the model can be evaluated by comparing T_p measured and T_p predicted for the data in the *training* set. In Fig. 4(a), the predicted T_p is plotted as a function of measured T_p. For a perfect model, the predicted T_p will be exactly the same as the measured T_p and all the data points will fall along the 45° diagonal line in our plot. In practice, there will be variations which are desirable so that we do not overfit the data. Thus, the training error (MSE^{train}), which can be calculated from Equation (3), is used to evaluate the performance of our model on the *training* data.

In general, how well the model works on the *training* data is not crucial. Rather, we are interested in the accuracy of the predictions that we obtain when we apply our model to unexplored *virtual* data. There are various methods to estimate the test error, which can be used to select the best model. Resampling methods repeatedly draw samples from a training data set and refit a model of interest on each sample to obtain additional information about the fitted model, for example, information to evaluate the performance of the model on unseen or test data.

Bootstrap resampling is commonly used to evaluate how robust a model is by assigning measures of accuracy to sample estimates. It relies on sampling with replacement and we utilize it to quantify the uncertainty associated with prediction from the statistical learning on the training data, i.e., to obtain the mean (μ) and standard error (σ) associated with the outcome of the model. Our training set contained $n = 53$ observations, from which we randomly selected n observations to produce a bootstrap data set. The sampling is performed with replacement, which means that the same observation can occur more than once in the bootstrap dataset. We trained a new LIN model on this bootstrap dataset, and made predictions for all the data points in the *training* dataset. We repeated this procedure 1000 times and obtained 1000 sets of predictions for the data in the *training* set for the mean (μ) and standard error (σ). The bootstrap results for our LIN model are shown in the inset to Fig. 4(a). The predicted T_p of y axis is the μ and error bar is the σ. To estimate the test error, we replaced the predicted value $\hat{y}_i$ with the mean value μ_i in Equation (3) to define a MSE^{boots} given by,

$$MSE^{boots} = \frac{1}{n} \sum_{i=1}^{n} (y_i - \mu_i)^2. \qquad (6)$$

Such an MSE^{boots} in some sense represents the test error of the
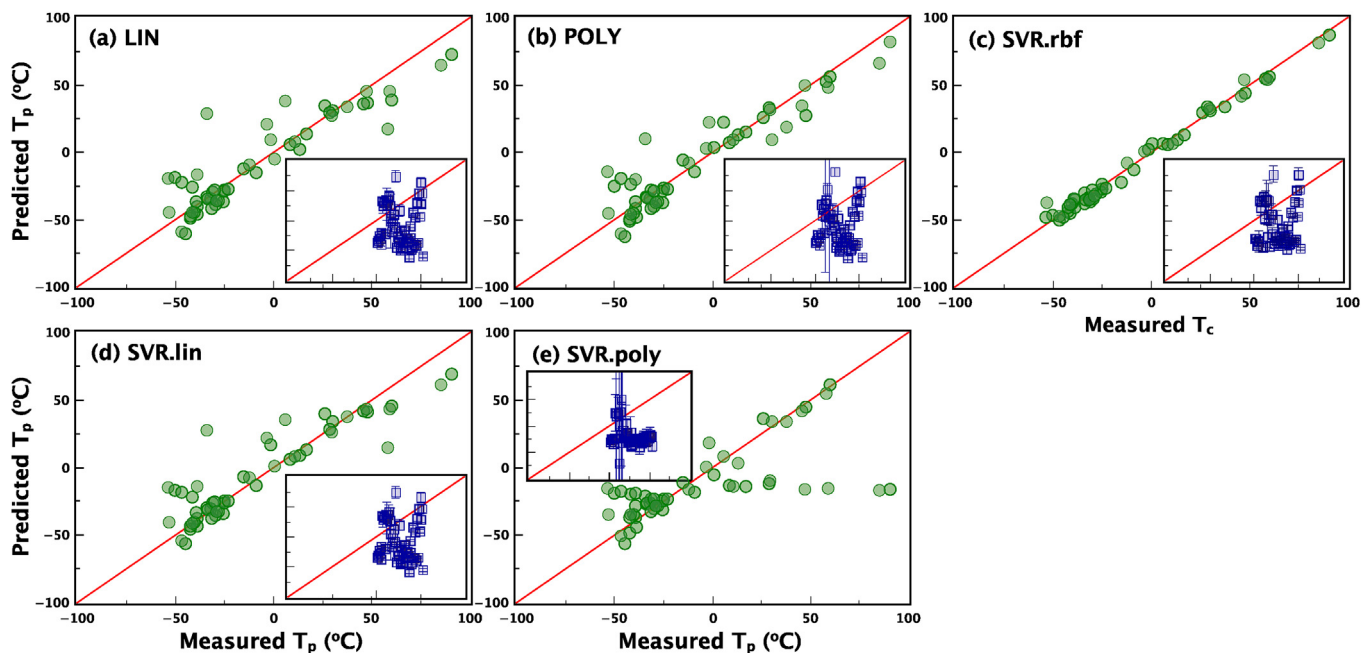

Fig. 4. The performance of the machine learning inference models on the *training* dataset. The predicted T_p values from the inference model are plotted as a function of measured T_p values. If the model is perfect, the predicted T_p will be exactly the same as the measured T_p and all the data points will align along the 45° diagonal line. The insets plot the mean (μ) and standard deviation (σ) of the predicted value from the inference model, obtained by bootstrap resampling from the initial 53 data points 1000 times. (a) linear regression (LIN); (b) polynomial regression (POLY); (c) Support vector regression with radial basis function kernel (SVR.rbf); (d) Support vector regression with linear kernel (SVR.lin); and (e) Support vector regression with polynomial kernel (SVR.poly).

model.

Cross-validation is used to assess the predictive capabilities of the model on unseen or test data. We typically hold-out a subset of the training observations from the fitting process and then apply the statistical learning model to the held-out observations. For our training set containing $n = 53$ observations, we fit the LIN model on $n - 1$ training observations, and the trained LIN model was used to predict $\hat{y}_m$ for the excluded observation (LOO, Leave One Out). Since the left out data point was not used in the fitting process, the squared error between this and the predicted value ($MSE = (y_m - \hat{y}_m)^2$) provides an approximate unbiased estimate for the test error. Repeating this approach n times on all the data points in turn, produces n squared errors and *CVerror*, the average of those errors, is given by

$$CVerror = \frac{1}{n} \sum_{m=1}^{n} (y_m - \hat{y}_m)^2 \qquad (7)$$

In the following, we train several models and compute their MSE^{train}, MSE^{boots}, and *CVerror*.

5.2. Model selection

Polynomial regression extends the linear model to higher powers in the features (e.g. cubic regression includes X, X^2, and X^3), and provides a simplified approach for non-linear fits to the data. To order d in the features *en*, *ven* and *dor*, we have $T_p = \beta_0 + \beta_1^{en}en + \beta_1^{dor}dor + \beta_1^{ven}ven + \ldots + \beta_d^{en}en^d + \beta_d^{dor}dor^d + \beta_d^{ven}ven^d$. The coefficients β_i^{en}, β_i^{ven}, and β_i^{dor} can be easily estimated using least squares regression. We tried different values of d for *en*, *dor* and *ven*, respectively, and each combination of d values for the three features corresponds to a polynomial model and determines its complexity. We used the cross-validation error, *CVerror*, to select the specific polynomial function for our targeted property, T_p. Fig. 5 shows the cross-validation error of each polynomial model as a function of the model complexity in terms of the sum of orders ($\sum d_i, i = en$, *dor* and *ven*). The red curve connects the best poly-nomial models for given complexity and *CVerror* decreases as the

order of the polynomial increases, revealing that the quality of the model improves. However, from the sum 6 onwards, there is little increase in *CVerror*. Given that we have a finite data size, we will clearly suffer from overfitting as the model complexity increases. There is thus a trade-off between retaining model simplicity and overfitting. As *CVerror* does not decrease appreciably from values of 4 onwards, and certainly increases from 6, we select the polynomial model corresponding to the sum of orders = 4. That is,

$$T_p = \beta_0 + \beta_1^{en}en + \beta_1^{dor}dor + \beta_1^{ven}ven + \beta_2^{dor}dor^2, \qquad (8)$$

which adds to the LIN model a quadratic term in *dor*. (This model has the lowest *CVerror* compared to the other possibilities with sum of orders = 4.) Later we will show that the quadratic term is important in predicting the transformation temperature T_p. Fig. 4(b) shows the predicted T_p as a function of measured T_p, indicating a much improved model. The means and errors from bootstrapped samples in the inset to Fig. 4(b) indicate that POLY is an improvement in terms of test error when compared to LIN.

Support vector regressors (SVRs) are kernel-based statistical learning approaches that are widely used in pattern recognition and imaging [34,35]. They use an implicit mapping Φ of the input data into a high-dimensional feature space defined by a kernel function, i.e., a function returning the inner product $< \Phi(x), \Phi(x') >$ between the images of two data points x, x_0 in the feature space. The learning then takes place in the feature space, and the data points only appear inside dot products with other points. We uti-lized SVR with a linear kernel (SVR.lin), radial basis function
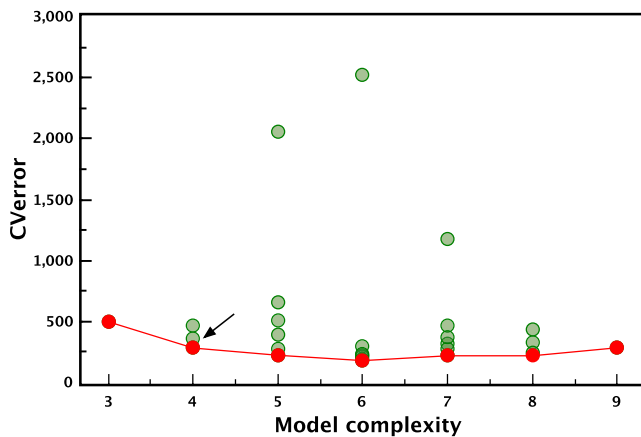

Fig. 5. Cross validation error for different polynomial models (filled circles) using the three features *en*, *ven* and *dor*. The x axis is the sum of the orders of the terms in the polynomial models (e.g. the linear model has terms of order 1 for the three fea-tures, thus the sum is 3.) and is a measure of the model complexity. Small cross validation error indicates goodness of the model. The higher the sum of orders, the more complex is the polynomial model. The red front tracks the best polynomial model for a given sum. We chose the best model for the sum of 4, to balance the trade-off between the goodness and model complexity. (For interpretation of the references to colour in this figure legend, the reader is referred to the web version of this article.)

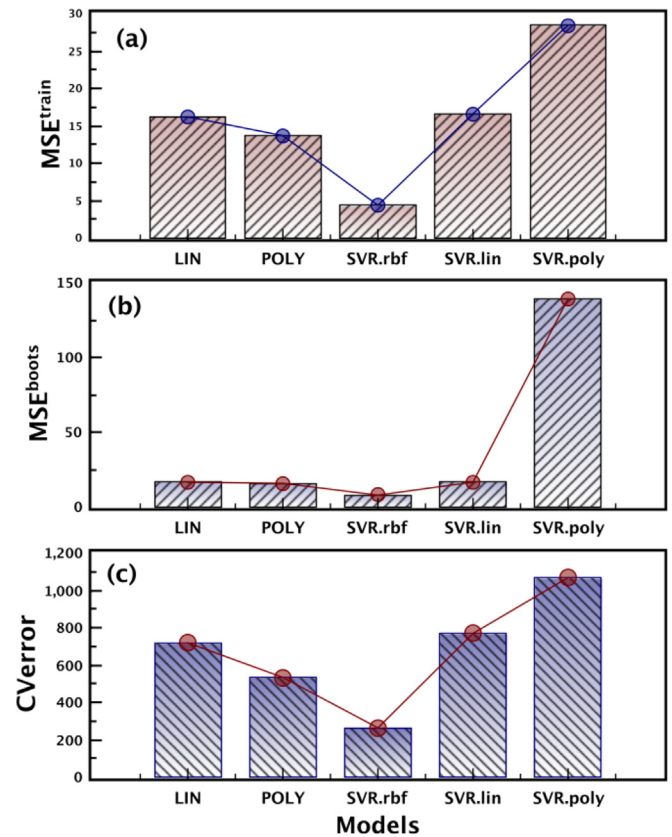**Fig. 6. Performance of different models on our *training* data in terms of MSE^{train}, MSE^{boots}, and *CVerror*.** (a) MSE^{train}, calculated using Equation (3), gives the training error for the inference model. (b) MSE^{boots} and (c) *CVerror*, computed by Equations (6) and (7), provide estimates of the test error. Form (a) to (c), SVR.rbf performs better than the others, POLY is next best.

(SVR.rbf) kernel, and polynomial kernel (SVR.poly). The meta-parameters for the SVR implementations were found using cross validation. Fig. 4 (c) - (e) show the performance of SVR.rbf, SVR.lin and SVR.poly models on our data. The SVR.rbf model performs very well on the data compared to SVR.lin or POLY; SVR.poly is the worst performer.

We computed the training and test errors for the above models, i.e., MSE^{train}, MSE^{boots}, and $CVerror$, using Equations (3), (6), (7). Fig. 6(a) shows MSE^{train} for five different models. It is clear that SVR.rbf out-performs all the other models, followed by POLY. Fig. 6(b) and (c) show MSE^{boots} and $CVerror$ estimates for the test errors with SVR.rbf out-performing all the other models with POLY next best. However, the outcome from SVR.rbf is not often easy to interpret and so to glean some understanding of the physics underlying the transformation temperature for SMAs, we will use the POLY model in the following.

5.3. Validation

Our *training* dataset is rather small and the estimates from MSE^{boots} and $CVerror$ of the test error for the *training* dataset may not accurately represent the full range of transformation temperatures. In addition, even though our machine learning models were built on the weighted atomic features, *en*, *ven* and *dor* for Ti$_{50}$(Ni$_{50-x-y-z}$ Cu$_x$ Fe$_y$ Pd$_z$), they are not restricted to those particular alloying elements and we can apply them to predict transformation temperatures of other alloying elements.

We therefore collected 23 data points from Frenzel et al. [9], who published a high precision dataset on the transformation temperatures of NiTi-based SMAs, with the constraint of Ti% = 50 as we are focusing on replacing Ni in the present study. Fig. 7(a)–(e) show how our model behaves on this 23 test data set. It appears that the LIN, POLY and SVR.lin perform fairly well for transformation temperatures below 100 °C. SVR.rbf behaves well only for about 8 data points, even though it is the best performing model based on MSE^{boots} and $CVerror$. Although SVR.poly predicts well the

high temperature data points, it is the POLY model that is quite predictive for the whole temperature range. Fig. 7 (f) shows the *MSE* error calculated from Equation (3) for the five models, indicating that the POLY model has the lowest error for the *test* data. The coefficients of the POLY model are shown in the first column of Table 2. Whether the same POLY model or one that is slightly different would apply to situations of varying Ti% is difficult to predict. However, we expect the features to be essentially the same.

Although we have an adequate model, such as POLY, a key question is what is the optimal design strategy for finding SMA alloys with targeted transformation temperatures ?

6. Adaptive design

We address this design problem by setting the goal of finding the highest transformation temperature alloy in our *virtual* dataset of unexplored alloys. We employed an adaptive design loop which uses a trade-off between exploration and exploitation of the results from our regressor model to guide the next experiment that needs to be performed [19–21]. The strategy we used is illustrated in Fig. 8 and it can be exercised using the following steps.

Steps 1 and 2 have already been discussed in Sections 2–5, where POLY is determined to be the inference model of choice. To find the highest T_p within our *virtual* dataset, we applied POLY to

Table 2
Coefficients of the POLY model on initial *training* dataset and updated *training* dataset.

	Initial		Updated	
	Estimate	Error	Estimate	Error
β_0	−7.76	1.97	−4.23	1.93
β_1^{en}	1819.54	139.21	2738.32	207.39
β_1^{dor}	−1676.79	132.68	−2495.48	202.57
β_2^{dor}	64.31	14.61	141.49	14.89
β_1^{ven}	−184.36	30.53	−184.59	30.21
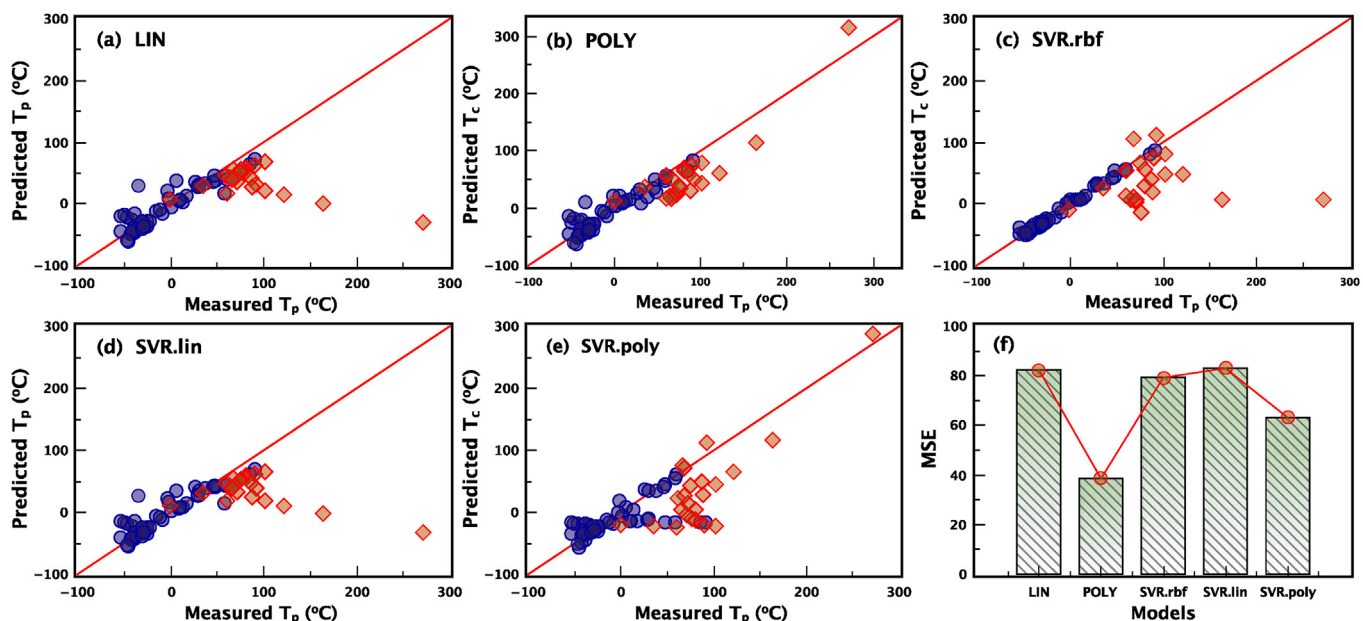
Fig. 7. The performance of the machine learning inference models on our *test* dataset. (a)–(e) The predicted T_p values from the inference model are plotted as a function of measured T_p values. The red points are from our *test* dataset and the blue points are from our *training* dataset. (f) Comparison of different models in terms of the *MSE* on the *test* dataset, suggesting the POLY is the best performing model. (For interpretation of the references to colour in this figure legend, the reader is referred to the web version of this article.)

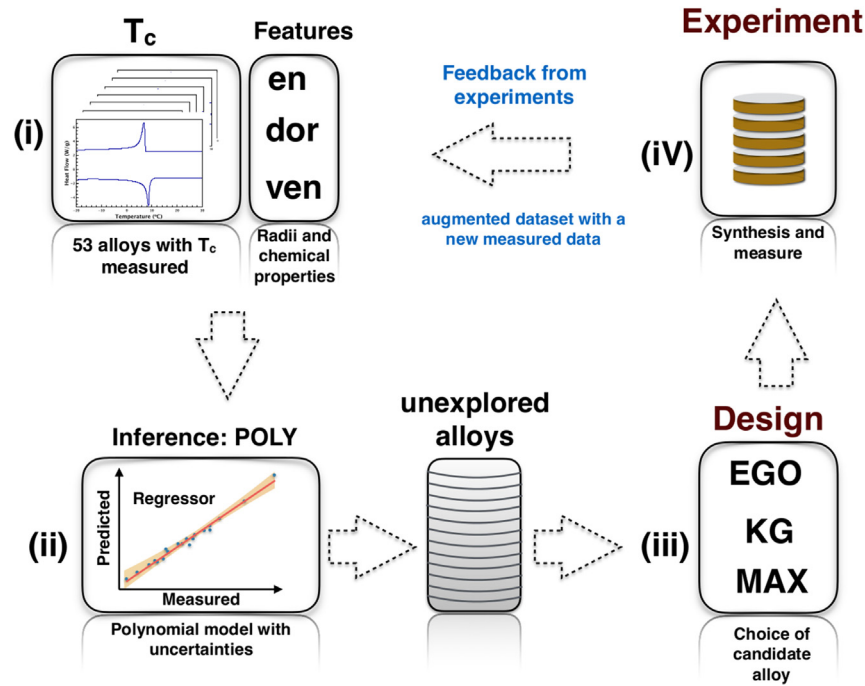**Fig. 8. Adaptive design loop.** (i) An initial experimental data set of 53 NiTi-based SMAs with known transformation temperature, and features (tabulated in Appendix) serves as input to the inference model. (ii) The model is trained and cross-validated with the initial alloy data. The trained model in (ii) is applied to a data set of unexplored alloys, defined as our *virtual* dataset. (iii) The design chooses the best candidate for synthesis and characterization. (iv) The measured transformation temperature augments the initial data set to further improve the inference and design.

1. Establish *training* and *virtual* datasets with features.
2. Learn an inference model for the relationship between features and the material property that we wish to optimize. It is important to consider uncertainties in the predicted properties.
3. Apply the trained inference model to the *virtual* dataset to predict property values with uncertainties of unexplored compounds.
4. Use a (*selector*) for *design* to suggest the next candidate material for experiment by balancing the trade-off between exploitation (choosing the material with the best predicted property) and exploration (using the predicted uncertainties to study regions of search space where the model is less accurate).
5. Improve iteratively the inference model by feeding back the measurement results from experiments.

estimate T_p for all 1,652,417 potential alloys (Step3). The mean (μ) and standard deviation (σ) of the predicted values were obtained by using *bootstrap resampling*, which considers representative random samples of some underlying distribution. The selectors choose or recommend the experiments which need to be performed next. In particular, the material to be synthesized next is selected to maximize the *Expected Improvement*, $EI(\mu, \sigma)$. Several selectors, all based on this concept, may be defined as follows:

- Max: $EI(\mu, \sigma) = \mu$: Greedily chooses the material with maximum predicted value.
- EGO (efficient global optimization): Maximizes the "expected improvement" $EI(\mu, \sigma) = \sigma[\phi(z) + z\Phi(z)]$, where $z = (\mu - \mu^*)/\sigma$ and μ^* is the maximum value observed so far in the training set. $\phi(z)$ and $\Phi(z)$ are the standard normal density and distribution functions, respectively.
- KG (knowledge gradient): $EI(\mu, \sigma) = \sigma[\phi(z) + z\Phi(z)]$, where $z = (\mu - \mu^{**})/\sigma$, where μ^{**} is the maximum value of either μ^* or μ'; μ' is the maximum predicted value in the virtual set.

We used these three *selectors* to choose the highest T_p alloy from our *virtual* dataset (Step4). The results are shown in Table 3. The *selector* Max chose $Ti_{50} Ni_{49.9} Cu_{0.1}$ as the best candidate, whereas *selectors* EGO and KG found that $Ti_{50} Ni_{25} Pd_{25}$ has the highest expected improvement and is the alloy to be synthesized next. The selection of EGO and KG is physically meaningful as it is known that adding Pd will increase the transformation temperature. The $Ti_{50} Ni_{25} Pd_{25}$ was then synthesized and its T_p was determined to be 182.89 °C. Our POLY model predicted a value of 189.56 °C, which is in good agreement. The new compound was added to our *training* dataset, which then contained 54 data points (Step5) and the POLY model was subsequently retrained on the updated *training* dataset. The coefficients of the updated POLY model are shown in the "updated" column of Table 2.

As seen in Table 3, the POLY model subsequently improved in terms of MSE^{train}, MSE^{boots} and *CVerror* after it was retrained with the new data. The three *selectors*, Max, EGO and KG then all converged to the same selection $Ti_{50} Ni_{25} Pd_{25}$, indicating no further room for improvement of T_p within the *virtual* dataset. The

Table 3
Comparison of the performance of POLY model on initial *training* dataset and updated *training* dataset and the predictions from initial POLY model and updated POLY model.

Data	Model: POLY			Selector: MAX		Selector: EGO		Selector: KG		Prediction
	MSE	MSE	CVerror	Alloy	Mean	Alloy	EI	Alloy	EI	$Ti_{50} Ni_{25} Pd_{25}$
Initial	13.7	15.7	356.2	$Ti_{50} Ni_{49.9} Cu_{0.1}$	81.2	$Ti_{50} Ni_{25} Pd_{25}$	258.5	$Ti_{50} Ni_{25} Pd_{25}$	258.5	189.56
Updated	13.5	15.0	224.0	$Ti_{50} Ni_{25} Pd_{25}$	125.5	$Ti_{50} Ni_{25} Pd_{25}$	113.5	$Ti_{50} Ni_{25} Pd_{25}$	113.5	183.41

predicted value from POLY model was 183.41 °C, an improvement on the previous value. In summary, we executed two iterations of the adaptive design iterative loop and the convergence suggests high efficiency of the design loop. Thus the adaptive design framework here can be used to accelerate the search for SMAs with targeted transformation temperatures.

7. Discussion and summary

As shown above, the POLY model reproduces the behavior of the transformation temperature in NiTi-based SMAs. It is then interesting to understand why the transformation temperature changes with the selected features and consequently with the alloying elements and concentration. We next consider a simple Landau-type model to reveal the reasons behind the influence of these features on the martensitic transformation temperature.

In general, the alloying elements have different atomic sizes from the host alloy elements. Therefore, we expect the doped elements with different sizes to give rise to local lattice strains. Such local strains contribute to the total free energy of the system, and we can model the effects of induced strain by alloying elements on the transformation temperature in terms of a Landau model. The one dimensional Landau-free energy for shape memory alloys can be written in the form [36].

$$F(T, \varepsilon) = \frac{1}{2}A(T - T_p)\varepsilon^2 + \frac{1}{4}B\varepsilon^4 + \frac{1}{6}C\varepsilon^6, \tag{9}$$

where A, B and C are elastic moduli of the materials (the later two are higher order moduli), T_p is the transformation temperature, and ε is the order parameter. When dopants replace the host atoms, a local strain e_d will be induced and will contribute to the total free energy by

$$F(T, \varepsilon) = \frac{1}{2}A(T - T_p)\varepsilon^2 + \frac{1}{4}B\varepsilon^4 + \frac{1}{6}C\varepsilon^6 + \alpha e_d^2 + \beta \varepsilon e_d, \tag{10}$$

where α and β are coefficients associated with local strain induced by doping. At equilibrium, $\frac{\partial F}{\partial e_d} = 0$, which gives,

$$e_d = -\frac{\beta}{2\alpha}\varepsilon. \tag{11}$$

As a result, the effective free energy is,

$$F(T, \varepsilon) = \frac{1}{2}A\left(T - T_p^*\right)\varepsilon^2 + \frac{1}{4}\varepsilon^4 + \frac{1}{6}\varepsilon^6, \tag{12}$$

where the T_p^* is the effective transformation temperature when doped with defects, and is given by

$$T_p^* = T_p + \frac{\beta^2}{2A\alpha}. \tag{13}$$

From Equation (13), it is clear that $\frac{\beta^2}{2A\alpha}$ is the transformation temperature change due to the dopant. Therefore, this change controlling the SMA transformation temperature is influenced by the modulus A and the local strains due to the effects of the atomic radii of the doped and host elements represented by β and α, respectively.

According to our POLY model, the transformation temperature linearly depends on the Pauling electronegativity (*en*) and valence electron number (*ven*) but quadratically depends on the *d*-orbital radii (*dor*). We selected *dor* to represent the atomic radii and thus this captures one aspect of the transformation temperature variation for different dopants. Moreover, the quadratic dependence of

transformation temperature on *dor* suggests that atomic radii may have even a stronger influence on the change in transformation temperature.

In our choice of features, the *en* and *ven* capture the chemical bonding properties. It is known that the strong bonding gives rise to large resistance to shape/volume change, and consequently results in high bulk and shear moduli. As the elastic modulus softens and reaches a constant critical value before transformation upon cooling, the elastic modulus of the parent phase influences the transformation temperature. If the elastic modulus of the parent phase is large, cooling should continue to lower temperatures before the critical point is reached; hence the transformation temperature is decreased. On the contrary, if the alloying elements lower the elastic modulus of the parent phase, the critical point can be reached at higher temperatures and the transformation temperature should increase. Thus, the introduction of alloying elements in NiTi is accompanied by a change in the elastic modulus as the interatomic metallic bonding is affected, which is captured by the features *en* and *ven*.

Various chemical and microstructural factors can affect the transformation temperature of SMAs, however, in the present study, we consider only compositional changes of the alloy. Other factors, including aging, precipitation, point defects, dislocations and degree of order, which are also critical in determining the transformation temperature, are closely related with processing conditions. We expect that the same machine learning strategy we have discussed here can be utilized to model the influence of processing conditions, to understand how they determine the transformation and how to control the transformation temperature with them.

In summary, we have demonstrated a systematic learning and adaptive design framework to guide the synthesis and discovery of new alloys with targeted transformation temperatures. The same strategy can be used to discover new materials with other desired properties.

Appendix A. Training data for the present study with features *en*, *ven* and *dor* and transition temperature T_p. The last sample is the new sample with highest transformation temperature.

Ti	Ni	Cu	Fe	Pd	*en*	*ven*	*dor*	T_p
50.0	45.2	1.0	3.8	0.0	1.7219	6.9340	0.4084	−25.44
50.0	44.4	2.0	3.6	0.0	1.7219	6.9480	0.4082	−33.92
50.0	42.8	4.0	3.2	0.0	1.7220	6.9760	0.4078	−41.59
50.0	43.6	3.0	3.4	0.0	1.7220	6.9620	0.4080	−31.27
50.0	46.0	0.0	4.0	0.0	1.7218	6.9200	0.4086	−39.10
50.0	44.5	1.5	3.0	1.0	1.7254	6.9550	0.4104	−50.27
50.0	34.0	13.0	0.0	3.0	1.7324	7.1300	0.4126	25.90
50.0	34.0	10.0	0.0	6.0	1.7414	7.1000	0.4202	30.20

(continued)

Ti	Ni	Cu	Fe	Pd	*en*	*ven*	*dor*	T_p
50.0	34.0	12.0	0.0	4.0	1.7354	7.1200	0.4151	37.60
50.0	42.0	5.0	3.0	0.0	1.7221	6.9900	0.4076	−46.59
50.0	35.0	12.0	0.0	3.0	1.7325	7.1200	0.4127	47.70
50.0	40.0	0.0	0.0	10.0	1.7540	7.0000	0.4312	5.77
50.0	34.0	14.0	0.0	2.0	1.7294	7.1400	0.4100	45.65
50.0	34.0	16.0	0.0	0.0	1.7234	7.1600	0.4049	60.10
50.0	44.0	1.0	1.0	4.0	1.7357	6.9900	0.4170	−34.13
50.0	34.0	0.0	0.0	16.0	1.7714	7.0000	0.4457	58.18
50.0	36.4	12.0	1.6	0.0	1.7225	7.0880	0.4061	13.24
50.0	41.2	6.0	2.8	0.0	1.7222	7.0040	0.4073	−53.50
50.0	38.0	10.0	2.0	0.0	1.7224	7.0600	0.4065	0.68
50.0	34.8	14.0	1.2	0.0	1.7226	7.1160	0.4057	−1.59
50.0	39.6	8.0	2.4	0.0	1.7223	7.0320	0.4069	−15.30
50.0	50.0	0.0	0.0	0.0	1.7250	7.0000	0.4070	90.85
50.0	44.0	2.0	4.0	0.0	1.7216	6.9400	0.4083	−53.33
50.0	44.5	2.1	3.4	0.0	1.7221	6.9530	0.4081	−25.11
50.0	44.0	2.3	3.6	0.1	1.7222	6.9510	0.4084	−32.05
50.0	40.4	4.6	1.0	4.0	1.7353	7.0260	0.4165	−3.33
50.0	45.7	0.0	4.3	0.0	1.7216	6.9140	0.4087	−42.17
50.0	45.8	0.0	4.2	0.0	1.7216	6.9160	0.4087	−38.83
50.0	42.8	3.6	2.8	0.8	1.7247	6.9800	0.4096	−39.05
50.0	43.9	2.1	4.0	0.0	1.7216	6.9410	0.4083	−40.34
50.0	44.5	1.7	3.7	0.1	1.7222	6.9430	0.4085	−28.04
50.0	45.7	1.2	3.0	0.1	1.7228	6.9520	0.4083	−9.08
50.0	44.0	2.3	3.7	0.0	1.7218	6.9490	0.4082	−39.36
50.0	45.1	1.4	3.5	0.0	1.7221	6.9440	0.4082	−25.31
50.0	44.6	1.9	3.4	0.1	1.7224	6.9510	0.4084	−23.08
50.0	43.8	2.6	3.6	0.0	1.7219	6.9540	0.4081	−33.57
50.0	43.9	1.5	4.6	0.0	1.7212	6.9230	0.4086	−44.91
50.0	44.5	1.9	3.4	0.2	1.7227	6.9510	0.4086	−30.05
50.0	46.0	1.1	2.8	0.1	1.7229	6.9550	0.4082	−12.22
50.0	43.8	2.0	4.1	0.1	1.7218	6.9380	0.4086	−42.23
50.0	43.9	2.0	4.0	0.1	1.7219	6.9400	0.4086	−41.48
50.0	46.8	0.9	2.0	0.3	1.7242	6.9690	0.4084	16.80
50.0	44.2	1.9	3.8	0.1	1.7221	6.9430	0.4085	−29.72
50.0	46.7	0.8	2.3	0.2	1.7237	6.9620	0.4083	8.62
50.0	44.2	1.9	3.9	0.0	1.7217	6.9410	0.4083	−31.29
50.0	48.1	0.2	1.5	0.2	1.7244	6.9720	0.4081	28.71
50.0	44.5	1.6	3.7	0.2	1.7225	6.9420	0.4088	−28.87
50.0	48.2	0.6	0.9	0.3	1.7251	6.9880	0.4080	47.19

Appendix B. Supplementary data

Supplementary data related to this article can be found at http://dx.doi.org/10.1016/j.actamat.2016.12.009.

References

[1] K. Otsuka, C. Wayman, Shape Memory Materials, Cambridge University Press, 1999. URL: https://books.google.com/books?id=DvItE9XUlN8C.

[2] K. Otsuka, T. Kakeshita, Science and technology of shape-memory alloys: new developments, Mrs Bull. 27 (2002) 91—100.

[3] J. San Juan, M.L. Nó, C.A. Schuh, Nanoscale shape-memory alloys for ultrahigh mechanical damping, Nat. Nanotechnol. 4 (2009) 415—419.

[4] J. Liu, T. Gottschall, K.P. Skokov, J.D. Moore, O. Gutfleisch, Giant magnetocaloric effect driven by structural transitions, Nat. Mater. 11 (2012) 620—626.

[5] Y. Song, X. Chen, V. Dabade, T.W. Shield, R.D. James, Enhanced reversibility and unusual microstructure of a phase-transforming material, Nature 502 (2013) 85—88.

[6] C. Chluba, W. Ge, R.L. de Miranda, J. Strobel, L. Kienle, E. Quandt, M. Wuttig, Ultralow-fatigue shape memory alloy films, Science 348 (2015) 1004—1007.

[7] J. Cui, Y.S. Chu, O.O. Famodu, Y. Furuya, J. Hattrick-Simpers, R.D. James, A. Ludwig, S. Thienhaus, M. Wuttig, Z. Zhang, et al., Combinatorial search of thermoelastic shape-memory alloys with extremely small hysteresis width, Nat. Mater 5 (2006) 286—290.

[8] M. Zarinejad, Y. Liu, Dependence of transformation temperatures of niti-based shape-memory alloys on the number and concentration of valence electrons, Adv. Funct. Mater. 18 (2008) 2789—2794.

[9] J. Frenzel, A. Wieczorek, I. Opahle, B. Maaß, R. Drautz, G. Eggeler, On the effect of alloy composition on martensite start temperatures and latent heats in ni—ti-based shape memory alloys, Acta Mater. 90 (2015) 213—231.

[10] K. Otsuka, X.B. Ren, Factors affecting the ms temperature and its control in shape-memory alloys, Mater. Sci. Forum 394 (2002) 177—184. Trans Tech Publ.

[11] X.B. Ren, K. Otsuka, Why does the martensitic transformation temperature strongly depend on composition? Mater. Sci. Forum 327 (2000) 429—432. Trans Tech Publ.

[12] J. Ma, I. Karaman, R.D. Noebe, High temperature shape memory alloys, Int. Mater. Rev. 55 (2010) 257—315.

[13] J. Frenzel, E.P. George, A. Dlouhy, C. Somsen, M.-X. Wagner, G. Eggeler, Influence of ni on martensitic phase transformations in niti shape memory alloys, Acta Mater. 58 (2010) 3444—3458.

[14] K. Otsuka, X. Ren, Physical metallurgy of ti—ni-based shape memory alloys, Prog. Mater. Sci. 50 (2005) 511—678.

[15] Y. Zhou, D. Xue, X. Ding, Y. Wang, J. Zhang, Z. Zhang, D. Wang, K. Otsuka, J. Sun, X. Ren, Strain glass in doped ti 50 (ni 50- xdx)(d= co, cr, mn) alloys: implication for the generality of strain glass in defect-containing ferroelectric systems, Acta Mater. 58 (2010) 5433—5442.

[16] Y. Zhou, D. Xue, X. Ding, K. Otsuka, J. Sun, X. Ren, High temperature strain glass transition in defect doped ti—pd martensitic alloys, Phys. Status Solidi (b) 251 (2014) 2027—2033.

[17] T. Honma, Types and mechanical characteristics of shape memory alloys, Shape Mem. Alloys (1984) 61—115.

[18] R. Zarnetta, R. Takahashi, M.L. Young, A. Savan, Y. Furuya, S. Thienhaus, B. Maaß, M. Rahim, J. Frenzel, H. Brunken, Y.S. Chu, V. Srivastava, R.D. James, I. Takeuchi, G. Eggeler, A. Ludwig, Identification of quaternary shape memory alloys with near-zero thermal hysteresis and unprecedented functional stability, Adv. Funct. Mater. 20 (2010) 1917—1923.

[19] D. Xue, P.V. Balachandran, J. Hogden, J. Theiler, D. Xue, T. Lookman, Accelerated search for materials with targeted properties by adaptive design, Nat. Commun. 7 (2016) 11241.

[20] D. Xue, P.V. Balachandrana, R. Yuan, T. Hu, X. Qian, E.R. Dougherty, T. Lookman, Accelerated search for batio3-based piezoelectrics with vertical morphotropic phase boundary using bayesian learning, Proc. Natl. Acad. Sci. 113 (47) (2016) 13301—13306.

[21] T. Lookman, P.V. Balachandran, D. Xue, J. Hogden, J. Theiler, Statistical inference and adaptive design for materials discovery, Curr. Opin. Solid State Mater. Sci. (2016), http://dx.doi.org/10.1016/j.cossms.2016.10.002.

[22] P. Raccuglia, K.C. Elbert, P.D. Adler, C. Falk, M.B. Wenny, A. Mollo, M. Zeller, S.A. Friedler, J. Schrier, A.J. Norquist, Machine-learning-assisted materials discovery using failed experiments, Nature 533 (2016) 73—76.

[23] S.R. Kalidindi, M. De Graef, Materials data science: current status and future outlook, Annu. Rev. Mater. Res. 45 (2015) 171—193.

[24] P.V. Balachandran, D. Xue, J. Theiler, J. Hogden, T. Lookman, Adaptive strategies for materials design using uncertainties, Sci. Rep. 6 (2016) 19660.

[25] P.V. Balachandran, D. Xue, T. Lookman, Structure—curie temperature relationships in batio 3-based ferroelectric perovskites: anomalous behavior of (ba, cd) tio 3 from dft, statistical inference, Exp. Phys. Rev. B 93 (2016) 144111.

[26] M. Fernandez, P.G. Boyd, T.D. Daff, M.Z. Aghaji, T.K. Woo, Rapid and accurate machine learning recognition of high performing metal organic frameworks for co2 capture, J. Phys. Chem. Lett. 5 (2014) 3056—3060.

[27] L. Pauling, The nature of the chemical bond. IV. The energy of single bonds and the relative electronegativity of atoms, J. Am. Chem. Soc. 54 (1932) 3570—3582.

[28] J.T. Waber, D.T. Cromer, Orbital radii of atoms and ions, J. Chem. Phys. 42 (1965) 4116—4123.

[29] D. Pettifor, Bonding and Structure in Molecules and Solids, Oxford, Oxford, 1995.

[30] N.N. Greenwood, A. Earnshaw, Chemistry of the Elements, second ed., Butterworth-Heinemann, 1997.

[31] E. Clementi, D.L. Raimondi, W.P. Reinhardt, Atomic screening constants from SCF functions. II. atoms with 37 to 86 electrons, J. Chem. Phys. 47 (1967) 1300—1307.

[32] K.M. Rabe, J.C. Phillips, P. Villars, I.D. Brown, Global multinary structural chemistry of stable quasicrystals, high-T_C ferroelectrics, and high-T_c superconductors, Phys. Rev. B 45 (1992) 7650—7676.

[33] G. James, D. Witten, T.J. Hastie, An Introduction to Statistical Learning : with Applications in R, Springer Texts in Statistics, Springer, New York, 2013. URL: http://opac.inria.fr/record=b1135511.

[34] C.J. Burges, A tutorial on support vector machines for pattern recognition, Data Min. Knowl. Discov. 2 (1998) 121—167.

[35] A.J. Smola, B. Schölkopf, A tutorial on support vector regression, Stat. Comput. 14 (2004) 199—222.

[36] G. Barsch, Landau theory of the displacive phase transformations in gold-cadmium and titanium-nickel alloys, Mater. Sci. Forum 327—328 (2000) 3570—3582.